

Infrared Spectroscopy of the Diffuse Ionized Halo of NGC 891

Richard J. Rand

*Department of Physics and Astronomy, University of New Mexico, 800 Yale Blvd, NE,
Albuquerque, NM 87131*

rjr@phys.unm.edu

and

Kenneth Wood

*School of Physics and Astronomy, University of St. Andrews, North Haugh, St. Andrews
KY16 9SS, UK*

kw25@st-andrews.ac.uk

Robert. A. Benjamin

*Department of Physics, University of Wisconsin at Whitewater, 800 West Main Street,
Whitewater, WI 53190*

benjamir@uww.edu

ABSTRACT

We present infrared spectroscopy from the *Spitzer Space Telescope* at one disk position and two positions at a height of 1 kpc from the disk in the edge-on spiral NGC 891, with the primary goal of studying halo ionization. Our main result is that the [Ne III]/[Ne II] ratio, which provides a measure of the hardness of the ionizing spectrum free from the major problems plaguing optical line ratios, is enhanced in the extraplanar pointings relative to the disk pointing. Using a 2D Monte Carlo-based photo-ionization code which accounts for the effects of radiation field hardening, we find that this trend cannot be reproduced by any plausible photo-ionization model, and that a secondary source of ionization must therefore operate in gaseous halos. We also present the first spectroscopic detections of extraplanar PAH features in an external normal galaxy. If they are in an exponential layer, very rough emission scale-heights of 330 – 530 pc are implied for the various features. Extinction may be non-negligible in the midplane and reduce these scale-heights significantly. There is little significant

variation in the relative emission from the various features between disk and extraplanar environment. Only the $17.4 \mu\text{m}$ feature is significantly enhanced in the extraplanar gas compared to the other features, possibly indicating a preference for larger PAHs in the halo.

Subject headings: galaxies: ISM — galaxies: spiral — galaxies: individual(NGC 891 — methods: numerical

1. Introduction

One of the most important changes in our way of thinking about interstellar gas in spiral galaxies in the past twenty years or so derives from the discovery that the ISM is much thicker than had been previously thought. Layers of great vertical extent (referred to as “extraplanar gas” or “gaseous halos”) have been found in just about every component of the ISM, especially in X-rays (e.g., Tüllmann et al. 2006b; Strickland et al. 2004), HI (e.g., Oosterloo, Fraternali, & Sancisi 2007), radio continuum (e.g., Dahlem, Lisenfeld, & Rossa 2006), diffuse ionized gas (DIG; e.g., Rossa & Dettmar 2003b; Rand 1996), and dust (Howk & Savage 1999; Alton et al. 1998, 2000). This gas may originate in star-formation driven disk-halo flows (e.g., Norman & Ikeuchi 1989), primordial infall (Chiappini, Matteucci, & Gratton 1997) or accretion from satellite galaxies (van der Hulst & Sancisi 2005). Evidence for a connection to star formation comes from the correlation of the brightness and extent of extraplanar DIG, X-ray, radio continuum and dust with the level of underlying disk star formation, both within and among galaxies (Rand 1996, 1998a; Rossa & Dettmar 2003a; Tüllmann et al. 2006a; Strickland et al. 2004; Dahlem et al. 2006; Howk & Savage 1999). On the other hand, some Galactic High Velocity Clouds have metallicities as low as $0.1 Z_{\odot}$ (Wakker 2004), which is not expected for gas originating in the disk.

1.1. Emission Lines from DIG

In the Milky Way, the DIG (or Reynolds Layer) accounts for most of the ionized ISM (Reynolds 1990), and represents a significant power requirement. Energetically, only photoionization by massive stars can comfortably explain the intensity of optical line emission (Reynolds 1990), which raises the question of how an ionizing source concentrated in a thin disk can be responsible for such thick ionized layers (Miller & Cox 1993; Dove & Shull 1994).

Much information regarding the source(s) of ionization have come from optical emission line ratios in the Milky Way and external galaxies (e.g., Rand 1997, 1998b; Greenawalt, Walterbos, & Braun

1997; Collins & Rand 2001; Otte, Gallagher, & Reynolds 2002; Haffner, Reynolds, & Tufté 1999; Hoopes & Walterbos 2003; Madsen, Reynolds, & Haffner 2006). Studies of the spatial behavior of several diagnostic line ratios have supported the idea that photo-ionization by massive stars is the primary ionization mechanism, but crucial aspects of the data require a more complex picture. The most characteristic result is that the ratios of $[\text{S II}]\lambda\lambda 6716, 6731$ and $[\text{N II}]\lambda\lambda 6548, 6583$ to $\text{H}\alpha$ generally increase with distance from the suspected ionizing source, in the Milky Way and in external galaxy disks and halos. This was initially interpreted as a fall in the ionization parameter, U , with distance from the ionizing source (e.g., Domgorgen & Mathis 1994; Rand 1998b) but more recently has been attributed to an increase in the gas temperature in the DIG relative to the immediate star forming environment due to a source of extra non-ionizing heating (e.g., Haffner et al. 1999; Otte et al. 2002, using further information from $[\text{O II}]\lambda 3727/\text{H}\alpha$ in edge-ons), while even more recently the importance of radiation field hardening during propagation (due to the longer mean free path for harder photons) has been stressed (Hoopes & Walterbos 2003; Wood & Mathis 2004, hereafter WM).

Measurements of other line ratios present further difficulties for a simple photo-ionization picture. In several external spiral galaxies, both edge-on and more face-on, $[\text{O III}]\lambda 5007/\text{H}\beta$ is found to increase, or at least vary little, with distance from the ionizing massive stars (e.g., Rand 1998b, 2000; Galarza, Walterbos, & Braun 1999; Otte et al. 2002; Hoopes & Walterbos 2003; Miller & Veilleux 2003). An increase has also been found in the Reynolds Layer for gas near the tangent point near $l = 27^\circ$ (Madsen & Reynolds 2005). This behavior is unexpected for dilute radiation fields and has led to the consideration of secondary sources of ionization, such as shocks, in many of the above-referenced studies. Extra non-ionizing heating in halos may also be a factor, although Collins & Rand (2001) find that this is an unlikely explanation in NGC 5775 and UGC 10288. Exceptions to this behavior of $[\text{O III}]/\text{H}\beta$ do exist, however (Tüllmann & Dettmar 2000; Miller & Veilleux 2003). $[\text{O I}]\lambda 6300/\text{H}\alpha$, which depends on the neutral fraction of H through a charge exchange reaction, when detected in the halos of edge-ons is generally enhanced relative to the disk (Rand 1998b, 2000; Miller & Veilleux 2003). It is very weak in the Reynolds Layer (Reynolds et al. 1998), and has only been detected in one external non-edge-on spiral, M33 (Voges & Walterbos 2006). $\text{He I}\lambda 5876$ is difficult to detect, but $\text{He I}/\text{H}\alpha$ traces the relative ionization fractions of helium and hydrogen and thus is a useful measure of the hardness of the radiation field. In the Milky Way, Madsen et al. (2006) have detected the line in a few diverse environments, finding a range of helium ionization fractions, but in general the diffuse gas is in a lower ionization state than in HII regions. The line is detected in M33 with large uncertainties (Hoopes & Walterbos 2003; Voges & Walterbos 2006), while in the halo of NGC 891 helium is about 70% ionized (Rand 1997).

Spectroscopy of the DIG in irregular galaxies has led to a similar picture, with massive stars being the main source of ionization, but shocks possibly contributing as well [based on observations of 15 such galaxies by Hunter & Gallagher (1997) and Martin (1997)].

In summary, then, although radiation from massive stars dominates the ionization of DIG, many other factors may be at play: non-ionizing heating, shocks or other secondary ionization sources, and radiation field hardening during propagation. In addition, photo-ionization structure will depend on the how the ionization parameter changes with distance from the massive stars, and on the mean stellar spectrum emerging from the star forming regions. Further complications arise from uncertainties in the halo gas abundances, and also of course from dust extinction, which is not insignificant even at distances 1–2 kpc from the midplane of several edge-on spirals, including particularly NGC 891 (Howk & Savage 1999, 2000, and references therein).

The Infrared Spectrograph (IRS; Houck et al. 2004) on board the *Spitzer Space Telescope* (Werner et al. 2004) opens a unique window on the ionization of diffuse gas through its access to infrared gas-phase lines, in particular the $12.81 \mu\text{m}$ [Ne II] and $15.55 \mu\text{m}$ [Ne III] lines, and in this paper we present mid-infrared spectra of the disk and halo of NGC 891. The ratio of these lines provides a diagnostic of ionization that is relatively insensitive to extinction, gas-phase abundances, and temperature (being low excitation lines in warm gas) – three of the biggest sources of confusion for the optical lines. The first two ionization potentials (IPs) of Ne are 21.6 and 41.0 eV. With fewer complications, this ratio should provide excellent constraints on whether the diffuse gas is purely photo-ionized or requires an additional source by comparing against models. The utility of these lines as ionization diagnostics in Galactic and extragalactic HII regions and starbursts was demonstrated using the *Infrared Space Observatory* (ISO) by, e.g., Thornley et al. (2000), Giveon et al. (2002), and Verma et al. (2003).

The aforementioned modeling by WM uses the 3D Monte-Carlo radiative transfer code of Wood, Mathis, & Ercolano (2004) to address several of the issues associated with photo-ionization. This code is able to employ more realistic geometries for the ambient gas – such as clumpy or fractal ISM distributions that may have a great impact on the ionization structure – than can be done by the 1D codes previously applied to the DIG problem (e.g., Domgorgen & Mathis 1994). It also incorporates radiation field hardening, non-ionizing heating, and a range of possible input spectra and luminosities. WM find that spectral hardening reduces the need for the non-ionizing heating source invoked by, e.g., Haffner et al. (1999), by producing higher gas temperatures and ratios of forbidden lines to Balmer lines, while suppressing He I emission. However, it is still not possible to match all of the line ratio data for the Reynolds layer and the halo of NGC 891 without invoking additional heating or

a secondary source of ionization. In this paper, we apply models tailored to the diffuse ISM density distribution of NGC 891 to constrain the sources of ionization using existing optical line ratios and the unique information provided by our *Spitzer* data.

1.2. Emission from PAH Features

Although our primary focus is on gas-phase lines, *Spitzer* spectroscopy also provides access to the mid-infrared spectral features that are generally attributed to polycyclic aromatic hydrocarbons (PAHs; Leger & Puget 1984; Allamandola, Tielens, & Barker 1985; Bakes, Tielens, & Bausch 2001a; Bakes et al. 2001b; Draine & Li 2007). The identification of individual large molecules, or families of such molecules, responsible for the various features, as well as their creation, destruction, heating and emission in different environments are all topics of current interest. Peeters, Spoon, & Tielens (2004) argue that PAH emission in general should be a good tracer of B stars. While PAH emission should be broadly connected to star formation, it is suppressed relative to the emission from larger grains in the immediate vicinity of recently formed stars (e.g, Lebouteiller et al. 2007). This is usually attributed to destruction of PAH molecules by harsh UV radiation fields. Wu et al. (2006) find that the equivalent widths (EW) of several PAH features are lower in BCDs than in typical starburst galaxies, and find a weak anticorrelation of PAH EWs with $[\text{Ne III}]/[\text{Ne II}]$. A stronger anticorrelation is found with a parameter given by this ratio multiplied by the UV luminosity and divided by the metallicity. Thus, hardness, radiation field intensity and metallicity may all bear on PAH chemistry and emission. In galaxy halos the hardness, at least in the 20–40 eV range, is traced by the $[\text{Ne III}]/[\text{Ne II}]$ ratio. The starlight intensity will clearly be weaker than in disks. As PAH emission is dominated by single-photon heating, their spectrum is not expected to vary with starlight intensity for the kinds of environments relevant here (Draine & Li 2007).

Further modification of the dust grain population may occur through sputtering, grain collisions, and other processes (Draine 2003). For instance, Jones, Tielens, & Hollenbach (1996) find that shocks, with speeds as low as 50 km s^{-1} , could be a source of PAHs through shattering of larger grains. Radiative acceleration of grains, with a size-dependent efficiency, may also cause a modification of the grain size population (Ferrara et al. 1991), with smaller grains staying closer to their formation sites (Davies et al. 1998). These effects could lead to differences in the grain population between disks and halos [see also Howk & Savage (1997) for a general discussion of processes that may lead to halo dust]. The vertical extent of PAH emission in halos and possible changes in the relative strengths of PAH features with height, and how these vary in galaxies with different star formation rates, could shed light on the

chemistry of these large molecules.

Here we report spectroscopic detections of PAHs at 11.2, 12.0, 12.7, 16.5, and 17.4 μm , and a broad plateau from 16.5 to 17.5 μm in the halo of an external normal spiral, for the first time (the first spectroscopic PAH detections in any external halo were by Engelbracht et al. (2006) for the starburst galaxy M82). PAHs emitting in this wavelength range are thought to be generally neutral and larger than PAHs emitting shortward of 10 μm (Draine & Li 2007). Features at 11–14 μm are thought to arise from C-H out-of-plane bending modes. The strong 11.2 μm feature is believed to arise from compact, condensed PAHs, while the 12.7 μm feature is thought to arise from more irregularly shaped molecules (van Dishoeck 2004). The red tail of the 11.2 μm feature is thought to arise mainly from cations (Hudgins & Allamandola 1999). van Dienenhoven et al. (2004) find that the shape of the 11.2 μm feature, in terms of the asymmetry of the blue and red sides, and the strength of the smaller feature at 11.0 μm , varies with the type of exciting source (i.e., HII regions, Herbig AeBe stars, young stellar objects and planetary nebulae).

Features in the 15–20 μm region have been discovered only recently. Moutou et al. (2000) first reported the 16.5 μm feature, in Galactic sources, while the 17.4 μm feature can be seen in the spectra of some of the Galactic sources observed by Van Kerckhoven et al. (2000) and was also tentatively seen in the nuclei of M82 and NGC 253 by Sturm et al. (2000). A broad plateau from 15 to 20 μm was found by Van Kerckhoven et al. (2000). Peeters et al. (2004) explore how these features change with the type of exciting source (i.e., HII regions, young stellar objects and evolved stars), and conclude that the discrete features in this wavelength range arise generally from prominent bands in neutral PAHs that should be larger than those responsible for the 10–15 μm features. while plateaus are due to blending of less prominent bands. They also find that the 17.4 μm feature may arise from several candidate PAHs. In the dust model of Draine & Li (2007), the PAHs responsible for this feature are also very large (300–10⁴ C atoms). Emission in this wavelength range from C-C-C bending modes of larger PAHs was predicted by Allamandola, Tielens, & Barker (1989).

As far as previous observations of PAH emission from galaxy halos are concerned, Irwin & Madden (2006), using archival ISO data for the edge-on NGC 5907, detect mid-infrared narrow-band emission well into the halo. They argue that PAH features should dominate the emission in the filters used, and thus that the PAHs in this halo have a typical scale-height of 3.5 kpc, with emission extending up to 6.5 kpc. NGC 5907 is a galaxy with a low star formation rate and little evidence for a DIG halo (Rand 1996). This result is therefore rather unexpected and needs to be confirmed.

Finally, PAH features from 6.2 to 11.2 μm in the disk of NGC 891 have already been detected by Mattila, Lehtinen, & Lemke (1999), who find variation in the band ratios along

the major axis, suggesting changes in the dehydrogenation degree and charge of the PAHs.

2. Observations

The data were taken on 2006 February 2 and 2006 March 4 (program ID 20380; PI: R. Rand) using the staring mode of the IRS Short-High (SH) module on board *Spitzer*. A log of the observations is given in Table 1. The SH module is a cross-dispersed echelle spectrograph providing spectral coverage from 9.9 to 19.6 μm with a resolving power of ≈ 600 . The aperture has dimensions of 4.7" x 11.3". In staring mode the SH module nods between two pointings centered 1/3 and 2/3 of the way along the slit.

Deep observations were made at locations in the halo of NGC 891 centered at a height of approximately $z = \pm 1$ kpc (hereafter “east halo” and “west halo” pointings) above a location in the disk at $R = 100''$ from the center of the galaxy. The reconstructed pointings indicate that the actual slit centers were at heights of 970 and 1120 pc on the east and west sides, respectively. A shorter observation of the disk location was also obtained. The exact coordinates of the pointings are given in Table 1, and the pointings are shown in Figure 1. The disk pointing falls between HII regions visible in Figure 1, although more embedded HII regions may contribute to the emission. The long integrations for the halo pointings meant that the data were divided into three Astronomical Observation Requests (AORs) per pointing, while the disk observation required only one AOR. Because of the bright infrared background, separate sky observations close in time to the target observations are necessary for IRS exposures of faint emission, particularly when the emission is expected to fill the slit. A deep sky exposure was taken on 2006 March 4 as part of this program. Unfortunately, the integration time is not as long as for the halo observations, resulting in the sky exposure dominating the noise in the halo spectra. No suitable sky exposure exists for the 2006 February 2 observations. However, only a small minority of the data were taken on this date (see Table 1) and since all lines of interest are detected with good sensitivity, these data were not used in the analysis.

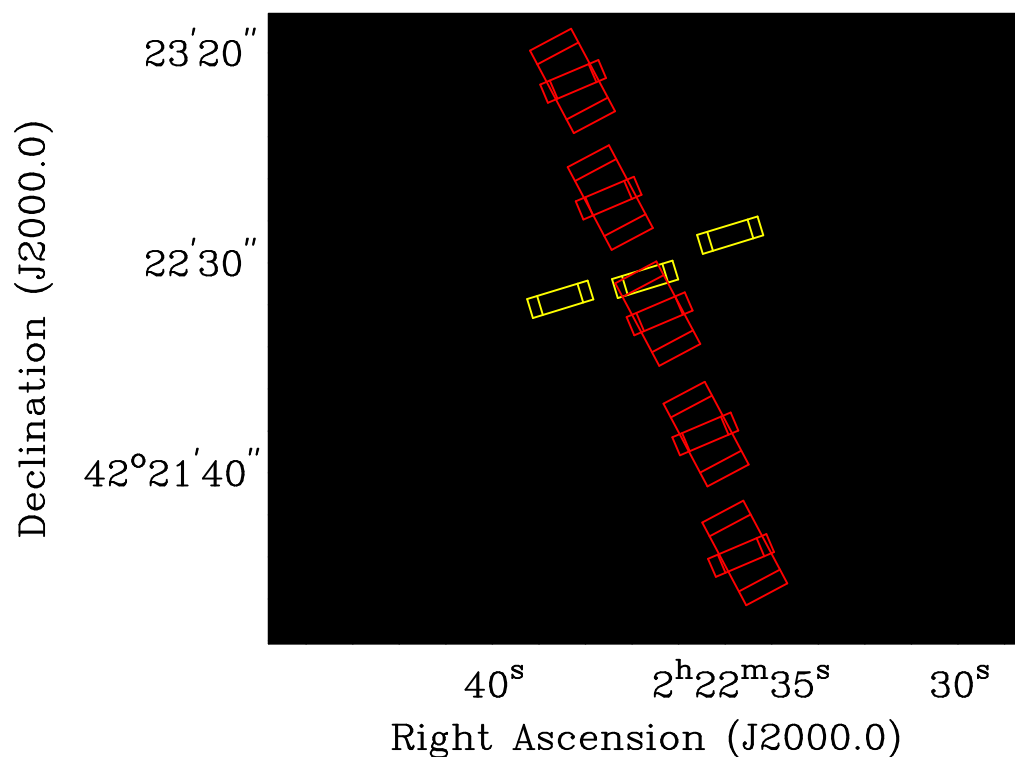


Fig. 1.— Section of an $H\alpha$ image of NGC 891 (Rand et al. 1990). Boxes show IRS pointings (for each pointing, two overlapping boxes, showing the two nodes, are drawn). The three (yellow) boxes closest to the long-slit are the IRS SH pointings discussed here. The other (red) boxes in the disk show pointings for the SH and LH GTO data discussed. The solid line shows the orientation of the slit for the optical emission line data discussed. The slit width is $2.25''$. The white blotch in the $H\alpha$ image is an artifact of continuum subtraction of a foreground star.

The data were processed through version S13.2 of the IRS reduction pipeline, providing the Basic Calibrated Data (BCD) products. Post-BCD processing was carried out according to the Infrared Spectrograph Data Handbook Version 2.0. Charge accumulation can be present in long integrations, evidenced by steady increases in the signal, but no significant effect was found in our data. The sky observation was subtracted from all target observations, and “rogue” pixels cleaned using the contributed IRSCLEAN_MASK software. For each of the AORs listed in Table 1 and for each nod, the 2-D spectra were averaged using sigma-clipping at the 3σ level. All remaining extreme pixels not removed by IRSCLEAN_MASK were replaced with averages of adjacent pixels. One-dimensional spectra were extracted using the package SPICE (version 1.3). Emission from NGC 891 is apparent over the entire aperture in every pointing, so the spectra were extracted and calibrated (with calibration tables, based on standard star observations, included in SPICE) using the full aperture width. Note that while version S13.2 of the pipeline allows extended source extraction, it is only fully accurate if the source uniformly fills the slit. The exact corrections for other emission distributions are impossible to estimate unless the source structure is known in advance. However, our comparison of our disk spectrum with nearby GTO pointings (see below) demonstrate that any such corrections will not affect the main results of this paper. A final spectrum for each pointing was formed by combining the resulting 1-D spectra for each AOR and nod. As the spectral orders overlap, the ends of each order were removed from the final spectra. The spectra are shown in Figure 2.

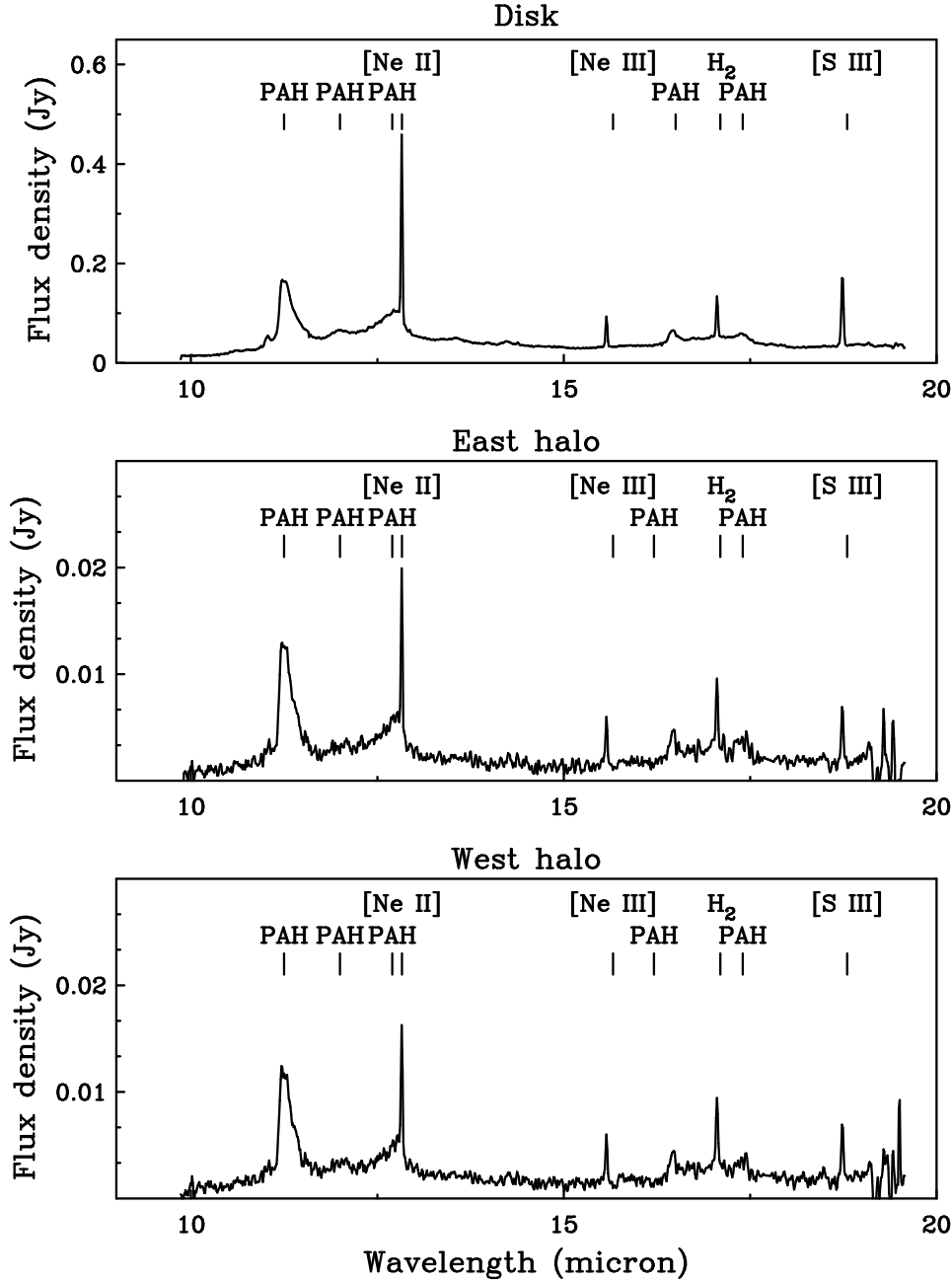


Fig. 2.— IRS SH spectra of the disk and east and west halo fields of NGC 891. Detected gas and dust phase features are indicated.

As we only had one disk pointing, we checked whether our gas-phase emission line ratios were representative by examining several pointings near our disk position in the Spitzer archive from GTO data, taken on 2004 August 7 (program ID 97; PI: J. Houck). Both SH and LH (covering 18.7–37.2 μm at a resolving power of ≈ 600 with an aperture of 11.1" x 22.3") data were reduced. These pointings, spaced by about 11" in R.A. and 28" in Decl., are also shown in Figure 1. Integration times per nod are 31.5 and 14.7 s for the SH and LH modules, respectively. We refer to these pointings as A to E, with A being southernmost. No dedicated sky observations exist for these pointings, so we used sky observations from 2004 August 8 (program ID 148). Because of the differing ecliptic latitude of these observations, the spectra had to be scaled to the expected sky level for the NGC 891 pointings using the predicted sky levels provided by the SPOT software before subtraction. Otherwise, the data were processed as above.

Line intensities and EWs were measured with the IRAF¹ program *plot* by summing pixels over the line extent and subtracting a linear baseline. Error bars on intensities are based on the noise in the spectra and the estimated uncertainties in the flux scale of IRS data, as described in the Infrared Spectrograph Data Handbook Version 2.0. Of the various sources of uncertainty in the flux scale, most affect the overall scaling independent of wavelength, while one is dependent on the position of the line in the order, and can be as much as 5%. We assume conservatively that it is everywhere at its maximum value. The total systematic error on intensities is then about 9%. The random noise in a single pixel is of order 10^{-17} erg cm^{-2} s^{-1} . For error bars on line ratios and EWs, we use only the random noise in the spectra and the wavelength-dependent error.

We checked that the fluxes in our halo pointings cannot be due to disk emission convolved with the PSF of the IRS SH module using the *Spitzer* contributed software STINYTIM. The emission in the disk pointing is peaked around the midplane. At a representative wavelength of 17 μm , we estimate that a point source in the midplane would contribute 0.04% of its peak intensity in our halo apertures due to the wings of the PSF, whereas the halo emission we detect for all features is at least 3% of the disk emission. Therefore we expect very little contamination from the disk in the halo pointings.

We also show optical emission line ratios in Figure 3 from the long-slit spectra of Rand (1998b). The observations are described in that paper.

¹IRAF is distributed by the National Optical Astronomy Observatory, which is operated by the Association of Universities for Research in Astronomy, Inc., under cooperative agreement with the National Science Foundation.

3. Results

3.1. Ionized Gas Phase Emission Lines

In all three pointings, we detect [Ne II] 12.81 μm , [Ne III] 15.56 μm , and [S III] 18.71 μm (Figure 2; Table 2). [S III] has an IP of 23.3 eV, similar to [Ne II]. We have also placed upper limits on [S IV] 10.51 μm emission. All of our disk line intensities fall between those for GTO pointings C and D (Table 3), as would naively be expected from the positions. To the extent that these limited measurements can be used to find the equivalent scale-height of an assumed exponential distribution of emission, the range of such scale-heights would be about 280 – 350 pc for [Ne II] and [S III], and 380 – 480 pc for [Ne III], given the error bars, and assuming no extinction (but see below). These change little if the average of the five intensities in the GTO data are used instead as a representative disk intensity. The [Ne III]/[Ne II] ratio is 0.13 ± 0.01 in the disk and 0.31 ± 0.03 and 0.32 ± 0.03 in the east and west halo, respectively (see also Figure 3a). For the five GTO pointings A–E, the [Ne III]/[Ne II] ratios are 0.12, 0.13, 0.14, 0.13 and <0.13 , respectively. For [S III]/[Ne III], we find ratios of 2.1 ± 0.2 in the disk and 0.8 ± 0.1 and 0.9 ± 0.1 in the east and west halo respectively. For GTO pointings A–E, the ratios are 1.9, 1.9, 2.0, 2.8 and < 3.2 , respectively. Hence, our disk results seem representative of the general trend in that part of the disk, while the two sides of the halo give similar ratios to each other. There is therefore a significant variation of these line ratios between the disk and the halo. Such variations we will refer to as halo-disk contrasts. There is no halo-disk contrast in [S III]/[Ne II], within the errors, consistent with their nearly equal IPs. The [Ne III]/[Ne II] results indicate a higher ionization state in the halo than in the disk. In §4 we explore whether this contrast can be explained by pure photo-ionization or whether a second source of ionization is required. We simply note here that the result cannot be explained by an additional non-ionizing source of heating in a pure photo-ionization model, as this ratio is temperature independent.

In a perfectly edge-on, gas rich disk such as NGC 891, extinction in the midplane may be significant even at mid-IR wavelengths. To estimate this effect, we calculate total gas column densities from the CO map of Scoville et al. (1993) and the HI map of Oosterloo et al. (2007). We calculate H₂ column densities from CO intensities assuming a conversion factor of $3 \times 10^{20} \text{ mol cm}^{-2} (\text{K km s}^{-1})^{-1}$, as used by Scoville et al. (1993). We assume the Galactic relation between A_V and gas column density from Bohlin et al. (1978), convert A_V to A_K using a standard Galactic reddening law (e.g., Draine 2003), and finally employ a value of $A_{15\mu\text{m}}/A_K$ of 0.4, consistent with determinations for many directions in the Galactic plane by Jiang et al. (2006). Extinction in this part of the spectrum is very uncertain and depends on the strength of the 18 μm silicate absorption feature, which, while clear in the ISO spectrum of the Galactic Center from Lutz (1999), is not evident in our disk spectrum.

Nevertheless, with these inputs we calculate about 2 magnitudes of extinction at $15\ \mu\text{m}$ at our disk position. Extinction at a $z = 1$ kpc is negligible. The possible effect of reddening on $[\text{Ne III}]/[\text{Ne II}]$ is even less well constrained. If we use the extinction at $12\ \mu\text{m}$ towards the Galactic Center from Lutz (1999), which exceeds that at $15\ \mu\text{m}$, the disk neon ratio would be further lowered.

Both disk and halo $[\text{Ne III}]/[\text{Ne II}]$ ratios are typical of nearby starburst galaxies studied by Thornley et al. (2000), and much lower than the HII regions 30 Doradus and W51 these authors compare against – a contrast they attribute to aging effects. However, these authors find that DIG is not likely to contribute much to their global ratios for starbursts. With increasing distance to the starburst, the $14''\times 27''$ ISO SWS aperture should encompass a greater fraction of diffuse gas. This led to the expectation of a decrease in the line ratio with starburst distance under the assumption of a lower ratio for DIG, and such a decrease is not observed by them. However, if the ratio generally increases with distance from ionizing stars, as found here, but with still relatively low values in the DIG, then such a trend might not be expected.

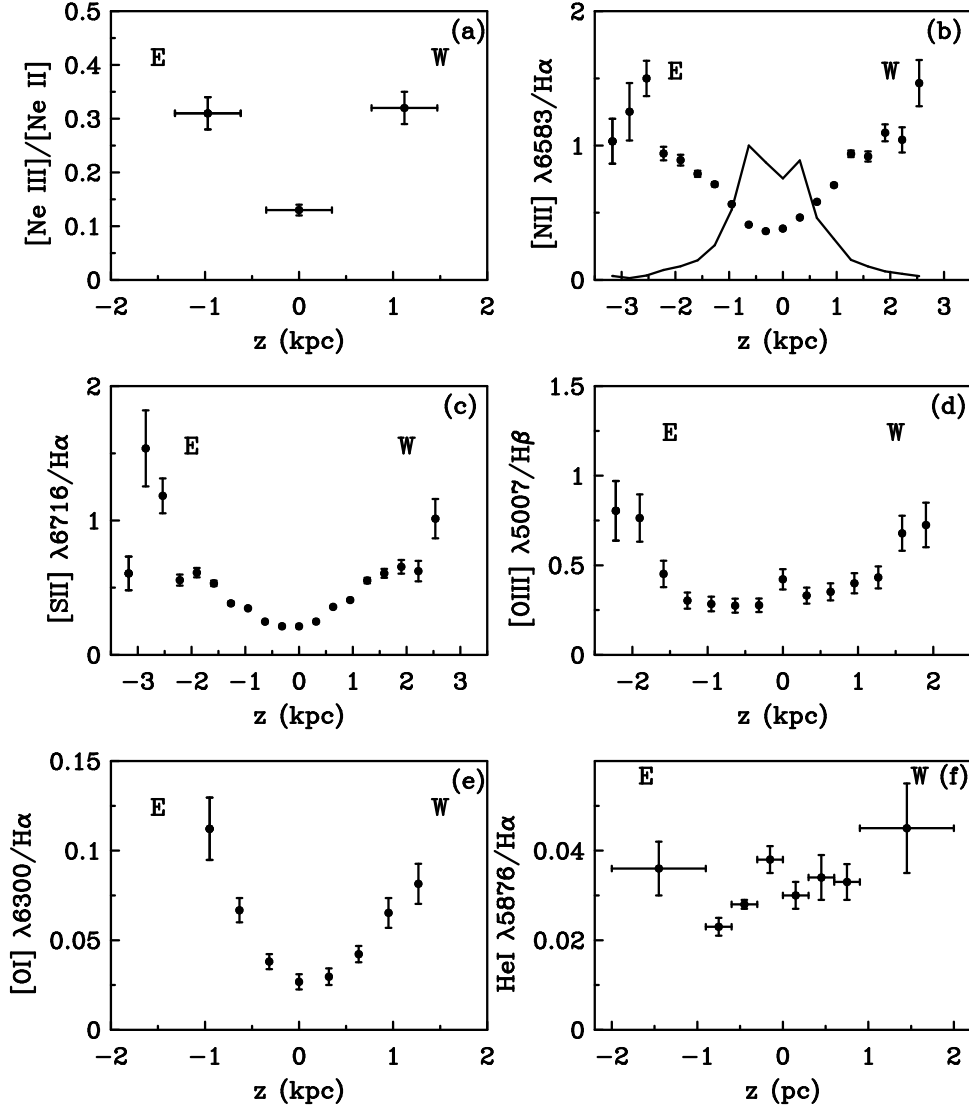


Fig. 3.— Dependence of (a) $[Ne\ III]/[Ne\ II]$, (b) $[N\ II]\lambda 6583/H\alpha$, (c) $[S\ II]\lambda 6716/H\alpha$, (d) $[O\ I]\lambda 6300/H\alpha$ (e) $[O\ III]\lambda 5007/H\beta$, and (f) $He\ I\ \lambda 5876/H\alpha$ on z . The optical line ratios are from Rand (1997) and Rand (1998b). The $H\alpha$ profile, normalized to unit intensity, from Rand (1998b), is shown in (b). Horizontal error bars in (a) and (f) reflect the extent over which the data have been averaged. In the other panels, the intensities were averaged over 317 pc.

3.2. PAH Emission Features

We detect five PAH features, at 11.2, 12.0, 12.7, 16.5 and 17.4 μm , and a broad plateau from roughly 16.5 to 17.5 μm (Figure 2; Table 2). The halo-disk emission contrasts of these five features as ordered above are 0.068 ± 0.006 , 0.04 ± 0.02 , 0.048 ± 0.011 , 0.056 ± 0.003 , and 0.14 ± 0.03 . Most features therefore have similar contrasts within the errors, consistent with the expectation that the PAH spectrum should not vary much with starlight intensity as long as it is not very strong. Only the 17.4 μm feature stands out as having a relatively high halo-disk contrast. The contrast for this line still stands out if the upper limits for the GTO data are used for the disk intensities (although upper limits on some other features complicate the comparison). It is also the only feature with a significantly higher EW in the halo (0.12 and 0.079 vs. 0.038), suggesting a larger vertical extent for this feature relative to the small, warm grains responsible for the continuum. Averaging the east and west halo measurements, the equivalent scale-heights of an assumed exponential distribution of emission would be about 330 – 530 pc for these features. For two magnitudes of extinction in the disk, the range becomes 210 – 270 pc. The scale-heights change little if we use instead the average of the disk intensities in the GTO observations (Table 3). For the 11.2 and 12.7 μm features (the only ones detected in all five GTO pointings), they become 460 and 380 pc, respectively, assuming no extinction. We also note for comparison that Mattila et al. (1999) found an intensity of the 11.2 μm feature of $2000 \pm 350 \text{ erg cm}^{-2} \text{ s}^{-1} \text{ arcsec}^{-2}$ for a $24'' \times 24''$ field centered at our disk position using ISO, somewhat larger than our value of $1400 \pm 100 \text{ erg cm}^{-2} \text{ s}^{-1} \text{ arcsec}^{-2}$, although the aperture sizes are not matched (again, the IRS SH aperture area is 53.11 arcsec^2).

CO emission at this location has a narrower vertical distribution. It is found to have a FWHM of about 225 pc in the high-resolution observations of Scoville et al. (1993), which would correspond to an exponential scale-height of 160 pc. Modeling of the HI disk by Oosterloo et al. (2007) reveals a thin disk with a scale-height of $<0.3 \text{ kpc}$ in the inner disk, rising to 0.5 kpc in the outer regions, and a thick disk with 30% of the HI mass, with a scale-height increasing with radius from 1.25 kpc to 2.5 kpc. The PAH features may therefore have a vertical distribution comparable to the main HI layer, but the extinction correction would make their distribution intermediate between the CO and HI layers.

Irwin & Madden (2006) modeled the vertical distribution of emission in NGC 5907 in the ISO 6.7W filter with one to three components. It is impossible to say whether there is one or indeed more vertical components to the PAH distribution from our data, but nevertheless one can state that if the PAH distribution in NGC 891 is represented by a single exponential distribution, then the range of FWHMs for the features of 450–730 pc, assuming no extinction, is less than that of even the narrowest component (830 pc) in NGC

5907 (in a model with three Gaussian layers). With our data we of course cannot rule out an extended tail to the PAH emission distribution with a scale-height of a few kpc as found for NGC 5907 by Irwin & Madden, but such an extended halo seems very unlikely in the more actively star-forming NGC 891.

Because four of the five PAH features show no significant halo-disk EW contrast, there is obviously no correlation with $[\text{Ne III}]/[\text{Ne II}]$. Note that we are only spanning a small range, and a lower regime, of this ratio compared to the BCD sample of Wu et al. (2006), where a weak correlation was found. However, the $17.4 \mu\text{m}$ EW is *higher* in the halo, where $[\text{Ne III}]/[\text{Ne II}]$ is higher – the opposite of the weak trend found by Wu et al. for the $6.2 \mu\text{m}$ and $11.2 \mu\text{m}$ features. The lack of EW halo-disk contrasts also puts limits on the modification of the grain size distribution by processes such as sputtering, shattering and radiative acceleration as discussed in §1.

Also as discussed in §1, the origin of the $17.4 \mu\text{m}$ feature is uncertain – it could arise from several relatively large, neutral, candidate PAHs (van Dishoeck 2004). The higher halo-disk contrast for this line may therefore indicate a halo favoring larger PAHs. Shattering of larger grains by shocks (Jones et al. 1996) in the halo is a potential source of such molecules.

The spectral resolution of the IRS SH module permits an analysis of the shapes of PAH emission feature profiles. The profiles of the $11.2 \mu\text{m}$ feature, after subtraction of a linear continuum interpolated across regions adjacent to the line, are shown in Figure 4 (the two sides of the halo have been averaged). The shape of this feature is found to vary with environment in the Milky Way by van Diedenhoven et al. (2004, see their Figure 3). Most common is the Class $A_{11.2}$ profile (relatively steep rise of the blue edge and fall of the red tail), typical of HII regions, non-isolated (i.e., associated with reflection nebulosity) Herbig AeBe stars and young stellar objects), while the Class $B_{11.2}$ (shallower rise of the blue edge, slightly redward shifted peak, shallower red tail, and the $11.0 \mu\text{m}$ secondary feature shifted redward and broadened) is shown by many planetary nebulae and post-AGB stars. A few sources feature a hybrid class $A(B)_{11.2}$ profile (similar to $A_{11.2}$ but with a shallower redward falloff and a slight redward shift of the $11.0 \mu\text{m}$ feature). In Figure 4, there is no discernible difference between the disk and halo profiles, suggesting little variation in the neutral/ionized mix or the excitation modes of the family of PAHs likely responsible for this feature. The profiles most resemble the $A_{11.2}$ type, with a relatively steep blue rise, shallow redward falloff, and a clear secondary feature at $11.05 \mu\text{m}$. The location of the peak of the secondary feature is more similar to that in the $A(B)_{11.2}$ profile. However, the main point is that there is no evidence for significant evolution of the PAHs responsible for the feature between the disk and halo.

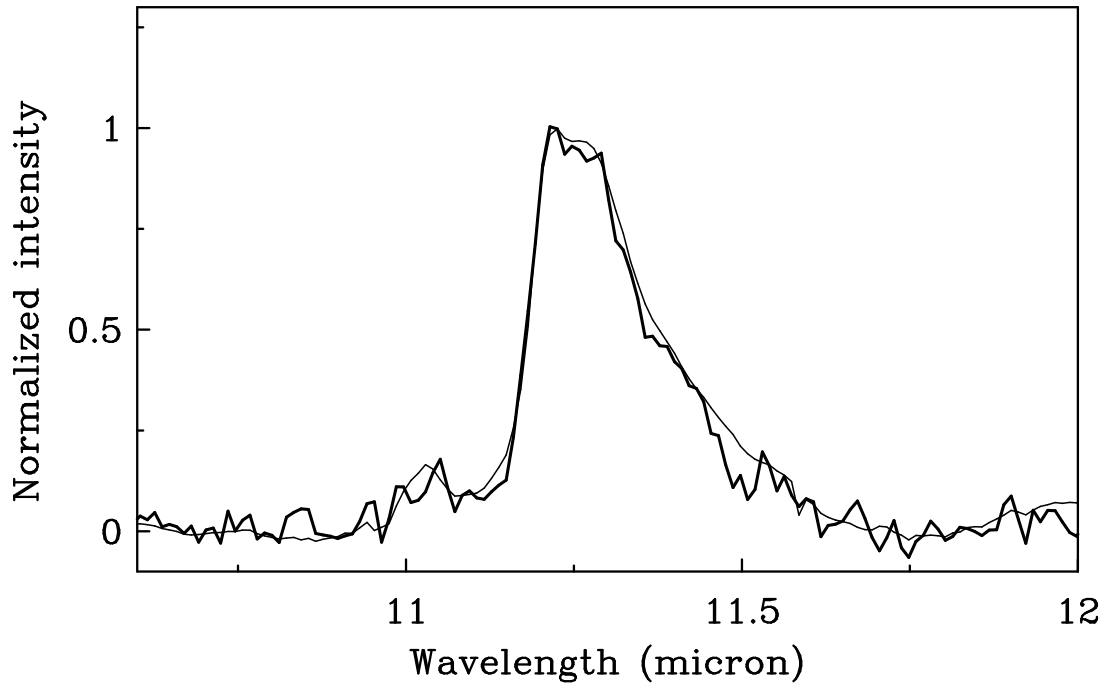


Fig. 4.— The 11.2 μm feature for the disk (solid line) and the average of the east and west halo pointings (dotted line). A linear continuum has been subtracted from the spectra.

The 15–18 μm emission features a broad plateau on which the 16.4 and 17.4 μm features sit. This part of the spectrum, after subtraction of a linear continuum using regions adjacent to the plateau, is shown in Figure 5 for the disk and the average of the two halo pointings. The location of the plateau, and the strengths of the two features relative to it and to each other, is much more reminiscent of the YSOs studied by Peeters et al. (2004) than the HII region in their sample. There is also a hint in the disk spectrum of the blue end of the second broad plateau seen in the spectrum of the ridge of H_2 near the Herbig Be star LKH α 234 by Peeters et al. from 18 to 20 μm , here seen as a shallow rise from 18 μ to 18.7 μm . Peeters et al. can reproduce both the HII region- and YSO-type profiles with mixes of laboratory PAH spectra, but the mixtures are not unique.

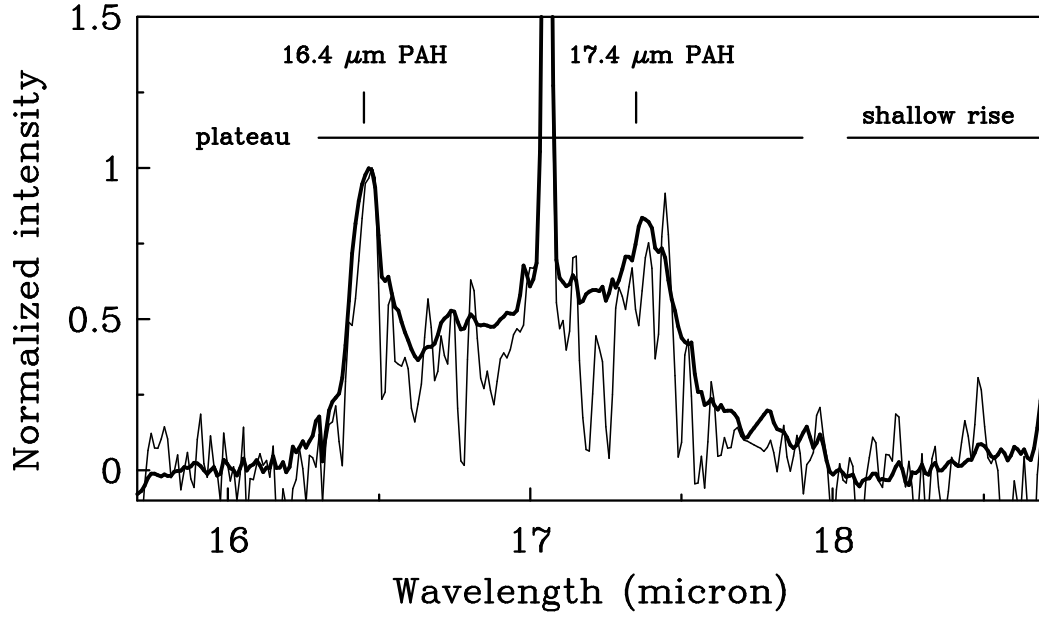


Fig. 5.— The 15–20 μm region for the disk (thick line) and the average of the east and west halo pointings (thin line). A linear continuum has been subtracted from the spectra.

3.3. H₂ Emission

H₂ mid-IR emission lines arise from rotational excitation in warm gas. It is usually attributed to PDRs (e.g., van Dishoeck 2004) but can also arise in shocks (e.g., Neufeld et al. 2006). Such emission has been mapped in the disk of NGC 891 using ISO Short-Wavelength Spectrometer (SWS) by Valentijn & van der Werf (1999). We detect the H₂ $S(1)$ $J = 3 - 1$ 17.03 μm rotationally excited line in the disk and halo. Our disk intensity is about 1.7 times higher than found for this line at the same position in the galaxy by Valentijn & van der Werf (1999), but the ISO SWS aperture size is not well matched to the IRS SH slit, being about seven times larger. Following the above analysis for the PAH features, if the emitting molecular hydrogen is in an exponential layer, then the measured halo-disk contrast suggests a scale-height of 390–460 pc. This result changes little if the GTO values are used. Again, extinction may lower the scale-height significantly: using our extinction estimate in §3.1 would bring the scale-heights down to 220 – 260 pc, still slightly thicker than the CO-emitting layer.

4. Ionization Modeling

Figure 3 includes not only the [Ne III]/[Ne II] ratio but also the optical line ratios along the long-slit (Figure 1) from Rand (1998b). We wish to understand if these line ratios can be reasonably reproduced by photo-ionization from a population of massive stars residing in the disk. We focus on models that predict at least semi-quantitatively the observed neon ratio first, given the aforementioned advantages of this ratio as an ionization diagnostic, and then examine how well such models reproduce the optical line ratios.

We calculated photo-ionization models using the 3D Monte Carlo photo-ionization code described in Wood et al. (2004). This code calculates the ionization and temperature structure for 3D distributions of gas and ionizing sources for elements H, He, C, N, O, Ne, and S. We do not consider ions with ionization potentials above 54 eV (the second ionization potential of He), therefore we do not consider He²⁺ or radiation transfer of photons with energies above 54 eV. This simplification is justified by the lack of detection of He²⁺ emission in the Reynolds layer and only its rare detection in HII regions. The models do not include the effects of dust on either the transfer of ionizing photons or the resulting line ratios. Observationally, from the CO and HI maps, modeling of the gas layers, and assumptions about extinction in §3.1, $A_V \approx 3$ mag at 500 pc above a position 100'' north of the galaxy center. Below this height, then, observed optical ratios may be somewhat affected by reddening. For instance, at 500 pc, the most reddened ratio, He I/H α , may be reddened by about 0.7 mag. Other ratios are for lines much more closely separated in wavelength.

For the bulk of the optical emission line data points in Figure 3, then, reddening should be insignificant and will not affect our conclusions. The simulations can include heating over and above that from photo-ionization, according to any given prescription (see WM), but we have not included additional heating in these simulations. The elemental abundances we adopt by number relative to H are: H/He = 0.1, C/H = 140 ppm, N/H = 75 ppm, O/H = 319 ppm, Ne/H = 117 ppm, and S/H = 18.6 ppm. With the exception of S, these are the gas phase abundances in the local ISM used by Mathis (2000). The S abundance we use was found by WM to better match Milky Way and NGC 891 data. Note that the calculated S line ratios are highly uncertain due to the unknown dielectronic recombination rates. In our simulations we use the dielectronic recombination rates for S suggested by Ali et al. (1991).

All models have a central ionizing source and ionize a simulation volume that extends to ± 1 kpc in x , y , and z , with 65 cubical grid cells on a side. The ionizing spectra are 40kK, 45kK, and 50kK model atmospheres from the WM-Basic library computed by Sternberg, Hoffmann, & Pauldrach (2003). The standard ionizing luminosity is 10^{51} H-ionizing photons per second, except in one model where we consider a luminosity four times higher. Also, for one simulation, we use a "leaky" model in which the input spectrum is that from a spherical 40kK simulation which has its physical size set to allow 15% of the ionizing photons to escape. This leaky model suppresses the He-ionizing photons with energies above 24.6 eV and hardens the spectrum in the H-ionizing continuum — see Figure 11 of WM and the accompanying discussion there.

The density structure within the simulation grid is given by

$$n(z) = 0.15 \exp[-|z|/0.66] + 0.04 \exp[-|z|/2.3] \quad (1)$$

where the densities are in cm^{-3} and distances are in kpc. This is a representative structure only, which we base on the HI data of Oosterloo et al. (2007) and Swaters et al. (1997). Our main results will not depend strongly on this assumed distribution.

We note that the models predict [O III]/H α while our data are for [O III]/H β . However, extinction should not affect the observed [O III]/H β since the lines are well matched in wavelength. Hence we expect trends with $|z|$ for [O III]/H α in the models to be comparable to those in [O III]/H β in the data.

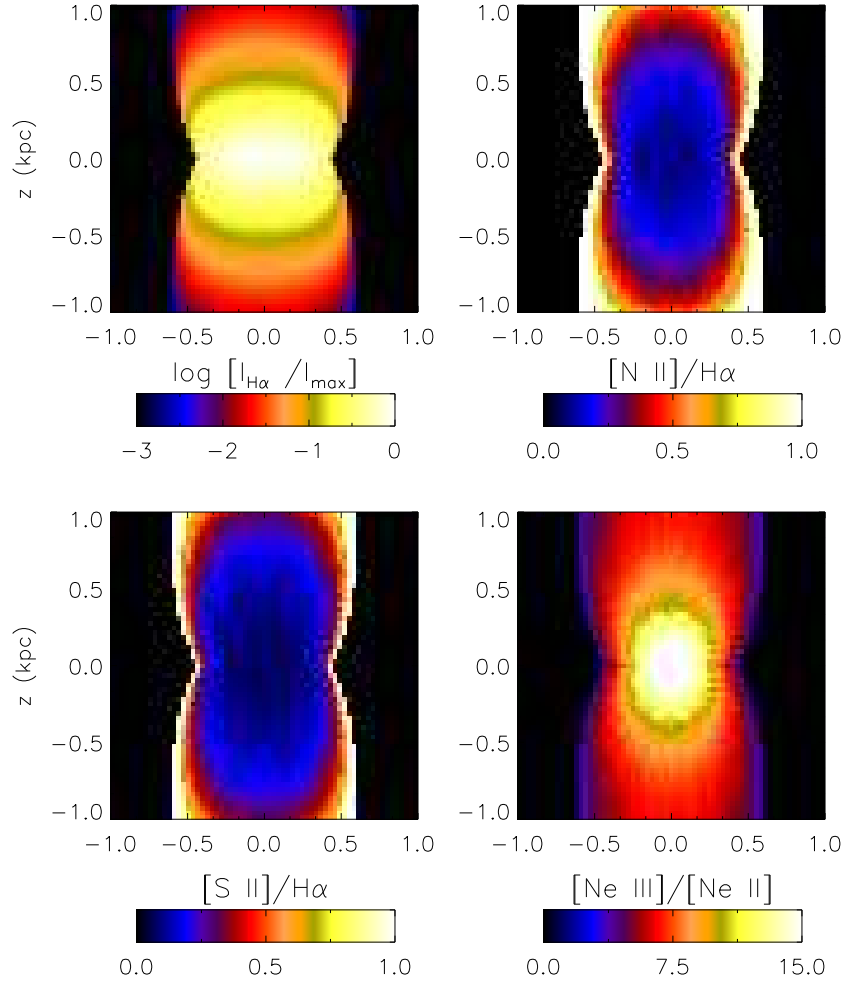


Fig. 6.— Total projected relative intensity and line ratio maps for $H\alpha$, $[N II]/H\alpha$, $[S II]/H\alpha$ and $[Ne III]/[Ne II]$ for a model with a 40kK ionizing source of luminosity 10^{51} H-ionizing photons per second.

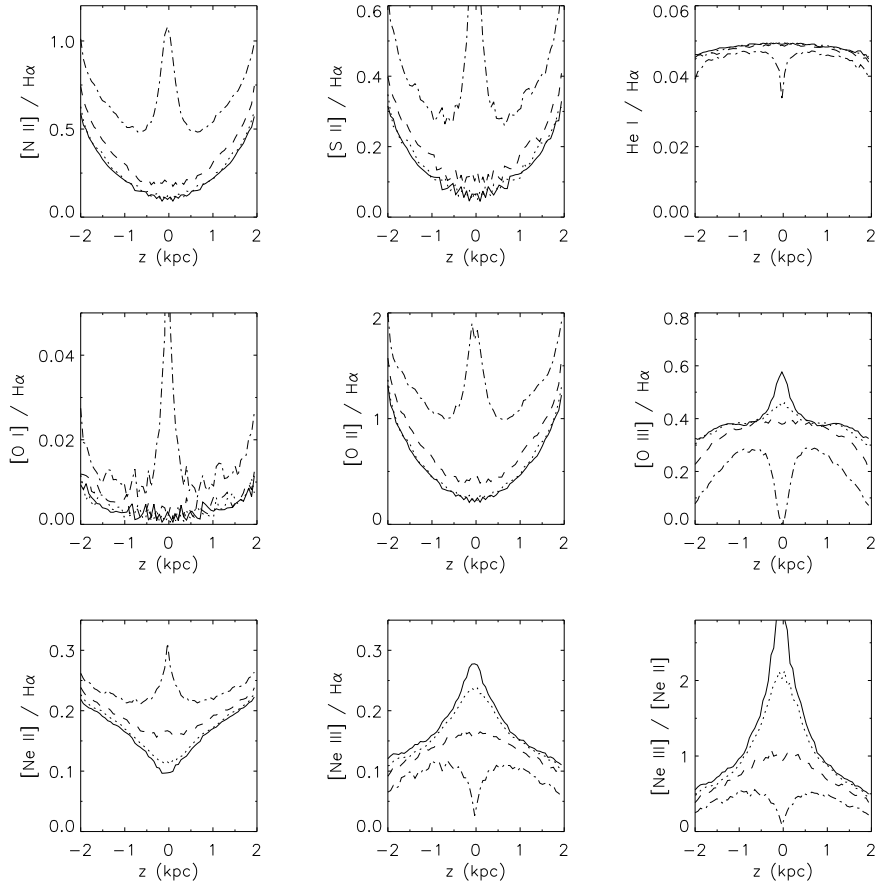


Fig. 7.— Vertical cuts at $x = 0$ kpc (solid), 0.3 kpc (dotted), 0.6 kpc (dashed) and 0.9 kpc (dot-dashed) showing the variation of line ratios with z for the model in Figure 6.

We illustrate trends in the models by first showing in Figure 6 2D maps of the $H\alpha$ intensity, $[\text{N II}]/H\alpha$, $[\text{S II}]/H\alpha$, and $[\text{Ne III}]/[\text{Ne II}]$ for our standard model with temperature 40kK. Vertical intensity cuts that show line ratios at x offsets of 0 kpc, 0.3 kpc, 0.6 kpc, and 0.9 kpc are shown in Figure 7. Figure 6 shows that the $[\text{N II}]/H\alpha$ and $[\text{S II}]/H\alpha$ ratios increase with distance from the ionizing source. This is due to the progressive hardening of the radiation field with increasing distance from the ionizing source (WM; Hoopes & Walterbos 2003). $[\text{Ne III}]/[\text{Ne II}]$ decreases with distance from the ionizing source due to the small number of high energy photons available at large distances to ionize Ne^+ to Ne^{2+} (only for the cut at $x = 0.9$ kpc do we see a hint of a rise in $[\text{Ne III}]/[\text{Ne II}]$ with $|z|$, but it is clear from Figure 6 that this is due to the idealized cone-like geometry of the simulations and cannot be considered a plausible match to the data; for the same reason, spikes and dips appear in most other line ratios at $|z| < 500$ pc for $x = 0.9$ kpc, in clear disagreement with the data). $[\text{O III}]/H\alpha$ falls with $|z|$, $\text{He I}/H\alpha$ is overpredicted and $[\text{O I}]/H\alpha$ is badly underpredicted for all cuts. The 50 kK model does produce $[\text{O III}]/H\alpha$ rising with $|z|$, but $[\text{Ne III}]/[\text{Ne II}]$ ranges from 6 to 20 and falls with $|z|$, while the situation for $\text{He I}/H\alpha$ and $[\text{O I}]/H\alpha$ is not improved.

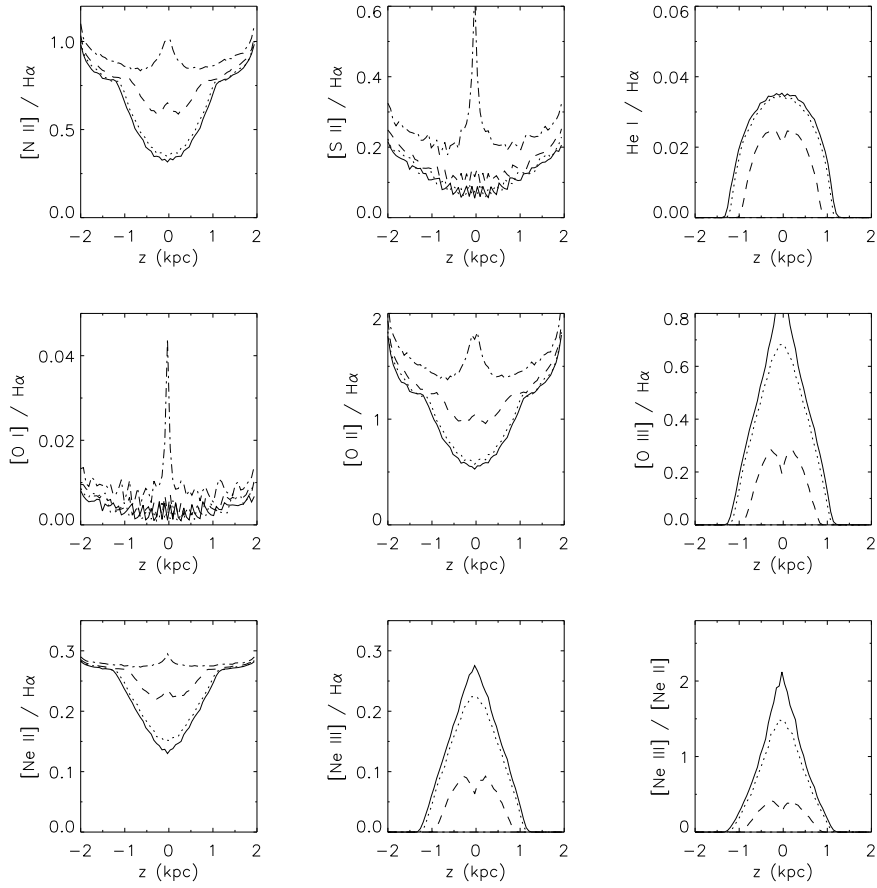


Fig. 8.— Vertical cuts at $x = 0$ kpc (solid), 0.3 kpc (dotted), 0.6 kpc (dashed) and 0.9 kpc (dot-dashed) showing the variation of line ratios with z for the 40 kK leaky model with luminosity 10^{51} H-ionizing photons per second.

The leaky 40kK model (Figure 8) shows falling $[\text{Ne III}]/[\text{Ne II}]$ with $|z|$ for all cuts. At $x = 0.9$, the values are at least comparable to the data. $[\text{O III}]/\text{H}\alpha$ and $\text{He I}/\text{H}\alpha$ still fall with $|z|$, again disagreeing with the data. Boosting the ionizing luminosity badly overpredicts $[\text{Ne III}]/[\text{Ne II}]$ and this ratio falls with $|z|$ between 0 and 1 kpc, while all optical ratios are badly matched. The leaky, high-luminosity 40kK model best matches the run of $\text{He I}/\text{H}\alpha$ (see discussion in WM), but again shows a neon ratio falling with $|z|$ and fails badly on the other optical ratios. In all the models considered here, $[\text{S III}]/[\text{Ne II}]$ (not shown) is badly overpredicted.

In summary, while the models can semi-quantitatively reproduce the behavior of $[\text{N II}]/\text{H}\alpha$ and $[\text{S II}]/\text{H}\alpha$, they generally overpredict $[\text{Ne III}]/[\text{Ne II}]$ and do not predict that this ratio should rise with $|z|$. Only at large distances in x from the ionizing source do the values begin to approach those observed (yet they still fall with $|z|$ in the model). The models also do not predict a rising $[\text{O III}]/\text{H}\alpha$ with $|z|$ as observed. The modeled $[\text{O I}]/\text{H}\alpha$ values are generally too low, and $\text{He I}/\text{H}\alpha$ is not well matched. These results demonstrate that hardening of the radiation field is insufficient to explain the data. An extra source of non-ionizing heating will also not affect the neon ratio as it is insensitive to gas temperature.

One potential explanation for enhanced $[\text{Ne III}]/[\text{Ne II}]$ in the halo would be the creation of higher levels of ionization due to increased collisional ionization. Such an enhancement could arise behind shocks in the halo. Although such shocks could not dominate the overall energetics of the diffuse ionized layers because of the large power requirements, they could provide the extra ionization at large heights above the disk. However, there are several difficulties with comparing our results to shock models. First, published models of steady-state shocks do not currently include predictions for infrared emission line intensities. Second, since these shocks are taking place in a low density medium, the length scales of the postshock cooling and recombination zones can be shown to approach the scale-height of the DIG. In such a case, it is necessary to consider the possibility of "truncated shocks" (Draine & McKee 1993) in which the integrated quantities are affected by the endpoint chosen for the recombination zone. Finally, given the hard radiation field produced by the postshock gas, the majority of the $[\text{Ne II}]$ and $[\text{Ne III}]$ that forms occurs in the postshock recombination zone. Thus the column densities should be sensitive to the presence and spectrum of the external radiation field. A more complete investigation of the sensitivity and role of shocks in affecting the ionization structure at high latitude will be included in subsequent investigations.

5. Conclusions

We have presented *Spitzer* IRS spectra of the disk and halo ($z = \pm 1$ kpc) of the edge-on spiral galaxy NGC 891. Our most important result is that the [Ne III]/[Ne II] ratio is found to be enhanced in the halo relative to the disk, and this is very difficult to reproduce in pure photo-ionization models.

Even this single observation presents a significant problem for models of DIG ionization featuring massive stars as the sole ionizing source. In a future paper we will explore shocks as a second source of ionization, but we remind the reader that other processes, such as cooling hot gas or turbulent mixing layers, may well be relevant and deserve further study.

We have detected several PAH features in the disk and the halo. If in exponential layers, their scale-heights are in the rough range 330–530 pc, probably between the CO and HI scale-heights. However, extinction in the disk may reduce these scale-heights significantly. Most have similar halo-disk emission contrasts, suggesting little variation in the PAH population, as expected for low starlight intensities. There is also very little halo-disk contrast in EW for most of the features, putting limits on modification between disk and halo of the relative numbers of PAHs and the very small grains responsible for the continuum. Only the 17.4 μm feature stands out as having a higher halo-disk contrast and a higher EW than the others, possibly indicating a preference for larger PAHs in halos, although the origin of this feature is uncertain. The information on PAHs in halos is limited so far, but such work on the vertical variations of the various emission features has great potential for understanding how interstellar processes can transport grains and modify their populations.

Our understanding of both the ionized gas and dust phases in halos will benefit from additional spectroscopic data in a range of halo environments, and we are in the process of acquiring such data with the IRS (program ID 40284; PI: R. Rand). In a future paper we will extend our NGC 891 data set with spectra at $z = \pm 2$ kpc, examine the halo of the more actively star-forming NGC 5775, where the rise of [O III]/H α with $|z|$ is even more problematic for pure photoionization models, and also the halo of NGC 3044, where a secondary ionization source is not evidently required, as [O III]/H α clearly falls with $|z|$ (Tüllmann & Dettmar 2000).

We thank G. Stacey for a brief but useful discussion about extinction in the mid-IR. We thank an anonymous referee for extensive comments which helped the paper significantly. This work is based (in part) on observations made with the Spitzer Space Telescope, which is operated by the Jet Propulsion Laboratory, California Institute of Technology under a contract with NASA. Support for this work was provided by NASA through an award issued

by JPL/Caltech.

Facilities: Spitzer Space Telescope.

REFERENCES

- Ali, B., Blum, R. D., Bumgardner, T. E., Cranmer, S. R., Ferland, G. J., Haefner, R. I., & Tiede, G. P. 1991, *PASP*, 103, 1182
- Allamandola, L. J., Tielens, A. G. G. M., & Barker, J. R. 1985, *ApJ*, 290, L25
- Allamandola, L. J., Tielens, G. G. M., & Barker, J. R. 1989, *ApJS*, 71, 733
- Alton, P. B., Bianchi, S., Rand, R. J., Xilouris, E. M., Davies, J. I., & Trewhella, M. 1998, *ApJ*, 507, L125
- Alton, P. B., Rand, R. J., Xilouris, E. M., Bevan, S., Ferguson, A. M., Davies, J. I., & Bianchi, S. 2000, *A&AS*, 145, 83
- Bakes, E. L. O., Tielens, A. G. G. M., & Bauschlicher, Jr., C. W. 2001a, *ApJ*, 556, 501
- Bakes, E. L. O., Tielens, A. G. G. M., Bauschlicher, Jr., C. W., Hudgins, D. M., & Allamandola, L. J. 2001b, *ApJ*, 560, 261
- Bohlin, R. C., Savage, B. D., & Drake, J. F. 1978, *ApJ*, 224, 132
- Chiappini, C., Matteucci, F., & Gratton, R. 1997, *ApJ*, 477, 765
- Collins, J. A., & Rand, R. J. 2001, *ApJ*, 551, 57
- Dahlem, M., Lisenfeld, U., & Rossa, J. 2006, *A&A*, 457, 121
- Davies, J. I., Alton, P., Bianchi, S., & Trewhella, M. 1998, *MNRAS*, 300, 1006
- Domgorgen, H., & Mathis, J. S. 1994, *ApJ*, 428, 647
- Dove, J. B., & Shull, J. M. 1994, *ApJ*, 430, 222
- Draine, B. T. 2003, *ARA&A*, 41, 241
- Draine, B. T., & Li, A. 2007, *ApJ*, 657, 810
- Draine, B. T., & McKee, C. F. 1993, *ARA&A*, 31, 373

- Engelbracht, C. W., Kundurthy, P., Gordon, K. D., Rieke, G. H., Kennicutt, R. C., Smith, J.-D. T., Regan, M. W., Makovoz, D., Sosey, M., Draine, B. T., Helou, G., Armus, L., Calzetti, D., Meyer, M., Bendo, G. J., Walter, F., Hollenbach, D., Cannon, J. M., Murphy, E. J., Dale, D. A., Buckalew, B. A., & Sheth, K. 2006, *ApJ*, 642, L127
- Ferrara, A., Ferrini, F., Barsella, B., & Franco, J. 1991, *ApJ*, 381, 137
- Galarza, V. C., Walterbos, R. A. M., & Braun, R. 1999, *AJ*, 118, 2775
- Giveon, U., Sternberg, A., Lutz, D., Feuchtgruber, H., & Pauldrach, A. W. A. 2002, *ApJ*, 566, 880
- Greenawalt, B., Walterbos, R. A. M., & Braun, R. 1997, *ApJ*, 483, 666
- Haffner, L. M., Reynolds, R. J., & Tufte, S. L. 1999, *ApJ*, 523, 223
- Hoopes, C. G., & Walterbos, R. A. M. 2003, *ApJ*, 586, 902
- Houck, J. R., Roellig, T. L., van Cleve, J., Forrest, W. J., Herter, T., Lawrence, C. R., Matthews, K., Reitsema, H. J., Soifer, B. T., Watson, D. M., Weedman, D., Huisjen, M., Troeltzsch, J., Barry, D. J., Bernard-Salas, J., Blacken, C. E., Brandl, B. R., Charmandaris, V., Devost, D., Gull, G. E., Hall, P., Henderson, C. P., Higdon, S. J. U., Pirger, B. E., Schoenwald, J., Sloan, G. C., Uchida, K. I., Appleton, P. N., Armus, L., Burgdorf, M. J., Fajardo-Acosta, S. B., Grillmair, C. J., Ingalls, J. G., Morris, P. W., & Teplitz, H. I. 2004, *ApJS*, 154, 18
- Howk, J. C., & Savage, B. D. 1997, *AJ*, 114, 2463
- . 1999, *AJ*, 117, 2077
- . 2000, *AJ*, 119, 644
- Hudgins, D. M., & Allamandola, L. J. 1999, *ApJ*, 516, L41
- Hunter, D. A., & Gallagher, III, J. S. 1997, *ApJ*, 475, 65
- Irwin, J. A., & Madden, S. C. 2006, *A&A*, 445, 123
- Jiang, B. W., Gao, J., Omont, A., Schuller, F., & Simon, G. 2006, *A&A*, 446, 551
- Jones, A. P., Tielens, A. G. G. M., & Hollenbach, D. J. 1996, *ApJ*, 469, 740
- Lebouteiller, V., Brandl, B., Bernard-Salas, J., Devost, D., & Houck, J. R. 2007, *ApJ*, 665, 390

- Leger, A., & Puget, J. L. 1984, *A&A*, 137, L5
- Lutz, D. 1999, in *ESA Special Publication*, Vol. 427, *The Universe as Seen by ISO*, ed. P. Cox & M. Kessler, 623–+
- Madsen, G. J., & Reynolds, R. J. 2005, *ApJ*, 630, 925
- Madsen, G. J., Reynolds, R. J., & Haffner, L. M. 2006, *ApJ*, 652, 401
- Martin, C. L. 1997, *ApJ*, 491, 561
- Mathis, J. S. 2000, *ApJ*, 544, 347
- Mattila, K., Lehtinen, K., & Lemke, D. 1999, *A&A*, 342, 643
- Miller, S. T., & Veilleux, S. 2003, *ApJ*, 592, 79
- Miller, W. W. I., & Cox, D. P. 1993, *ApJ*, 417, 579
- Moutou, C., Verstraete, L., Léger, A., Sellgren, K., & Schmidt, W. 2000, *A&A*, 354, L17
- Neufeld, D. A., Melnick, G. J., Sonnentrucker, P., Bergin, E. A., Green, J. D., Kim, K. H., Watson, D. M., Forrest, W. J., & Pipher, J. L. 2006, *ApJ*, 649, 816
- Norman, C. A., & Ikeuchi, S. 1989, *ApJ*, 345, 372
- Oosterloo, T., Fraternali, F., & Sancisi, R. 2007, *AJ*, 134, 1019
- Otte, B., Gallagher, III, J. S., & Reynolds, R. J. 2002, *ApJ*, 572, 823
- Peeters, E., Spoon, H. W. W., & Tielens, A. G. G. M. 2004, *ApJ*, 613, 986
- Rand, R. J. 1996, *ApJ*, 462, 712
- . 1997, *ApJ*, 474, 129
- . 1998a, *Publications of the Astronomical Society of Australia*, 15, 106
- . 1998b, *ApJ*, 501, 137
- . 2000, *ApJ*, 537, L13
- Rand, R. J., Kulkarni, S. R., & Hester, J. J. 1990, *ApJ*, 352, L1
- Reynolds, R. J. 1990, *ApJ*, 349, L17
- Reynolds, R. J., Hausen, N. R., Tufte, S. L., & Haffner, L. M. 1998, *ApJ*, 494, L99+

- Rossa, J., & Dettmar, R.-J. 2003a, *A&A*, 406, 493
- . 2003b, *A&A*, 406, 505
- Scoville, N. Z., Thakkar, D., Carlstrom, J. E., & Sargent, A. I. 1993, *ApJ*, 404, L59
- Sternberg, A., Hoffmann, T. L., & Pauldrach, A. W. A. 2003, *ApJ*, 599, 1333
- Strickland, D. K., Heckman, T. M., Colbert, E. J. M., Hoopes, C. G., & Weaver, K. A. 2004, *ApJS*, 151, 193
- Sturm, E., Lutz, D., Tran, D., Feuchtgruber, H., Genzel, R., Kunze, D., Moorwood, A. F. M., & Thornley, M. D. 2000, *A&A*, 358, 481
- Swaters, R. A., Sancisi, R., & van der Hulst, J. M. 1997, *ApJ*, 491, 140
- Thornley, M. D., Schreiber, N. M. F., Lutz, D., Genzel, R., Spoon, H. W. W., Kunze, D., & Sternberg, A. 2000, *ApJ*, 539, 641
- Tüllmann, R., Breitschwerdt, D., Rossa, J., Pietsch, W., & Dettmar, R.-J. 2006a, *A&A*, 457, 779
- Tüllmann, R., & Dettmar, R.-J. 2000, *A&A*, 362, 119
- Tüllmann, R., Pietsch, W., Rossa, J., Breitschwerdt, D., & Dettmar, R.-J. 2006b, *A&A*, 448, 43
- Valentijn, E. A., & van der Werf, P. P. 1999, *ApJ*, 522, L29
- van der Hulst, J. M., & Sancisi, R. 2005, in *ASP Conf. Ser. 331: Extra-Planar Gas*, ed. R. Braun, 139–+
- van Dienenhoven, B., Peeters, E., Van Kerckhoven, C., Hony, S., Hudgins, D. M., Allamandola, L. J., & Tielens, A. G. G. M. 2004, *ApJ*, 611, 928
- van Dishoeck, E. F. 2004, *ARA&A*, 42, 119
- Van Kerckhoven, C., Hony, S., Peeters, E., Tielens, A. G. G. M., Allamandola, L. J., Hudgins, D. M., Cox, P., Roelfsema, P. R., Voors, R. H. M., Waelkens, C., Waters, L. B. F. M., & Wesselius, P. R. 2000, *A&A*, 357, 1013
- Verma, A., Lutz, D., Sturm, E., Sternberg, A., Genzel, R., & Vacca, W. 2003, *A&A*, 403, 829
- Voges, E. S., & Walterbos, R. A. M. 2006, *ApJ*, 644, L29

Wakker, B. P. 2004, *Ap&SS*, 289, 381

Werner, M. W., Roellig, T. L., Low, F. J., Rieke, G. H., Rieke, M., Hoffmann, W. F., Young, E., Houck, J. R., Brandl, B., Fazio, G. G., Hora, J. L., Gehrz, R. D., Helou, G., Soifer, B. T., Stauffer, J., Keene, J., Eisenhardt, P., Gallagher, D., Gautier, T. N., Irace, W., Lawrence, C. R., Simmons, L., Van Cleve, J. E., Jura, M., Wright, E. L., & Cruikshank, D. P. 2004, *ApJS*, 154, 1

Wood, K., & Mathis, J. S. 2004, *MNRAS*, 353, 1126

Wood, K., Mathis, J. S., & Ercolano, B. 2004, *MNRAS*, 348, 1337

Wu, Y., Charmandaris, V., Hao, L., Brandl, B. R., Bernard-Salas, J., Spoon, H. W. W., & Houck, J. R. 2006, *ApJ*, 639, 157

Table 1. NGC 891 IRS Observations^a

AOR	Date (2006)	Pointing ^b	R.A. (J2000.0)	Decl. (J2000.0)	Integ. time per nod (sec)
14595584	March 4	Disk	2 ^h 22 ^m 36.8 ^s	42° 22' 27''	2x480
14595840	March 4	Sky	2 ^h 23 ^m 6.4 ^s	42° 22' 27''	1x480
14596096	March 4	Halo East	2 ^h 22 ^m 38.6 ^s	42° 22' 22''	9x480
14596352	March 4	Halo East	2 ^h 22 ^m 38.6 ^s	42° 22' 22''	9x480
14596608	Feb 2 ^C	Halo East	2 ^h 22 ^m 38.6 ^s	42° 22' 22''	7x480
14596864	March 4	Halo West	2 ^h 22 ^m 35.0 ^s	42° 22' 38''	9x480
14597120	March 4	Halo West	2 ^h 22 ^m 35.0 ^s	42° 22' 38''	9x480
14597376	March 4	Halo West	2 ^h 22 ^m 35.0 ^s	42° 22' 38''	7x480

^aSpitzer program ID 20380

^bPointing center of the field of view (each nod pointing is symmetrically offset from this position)

^cThese data are not used

Table 2. Infrared Line Intensities and PAH Equivalent Widths

Line	Disk Intensity ^a	Disk EW (μm)	Halo East Intensity	Halo East EW (μm)	Halo West Intensity	Halo West EW (μm)
[SIV] 10.51 μm	<1.9 ^b		<1.0		<1.1	
[Ne II] 12.81 μm	320 \pm 20		12 \pm 1		11 \pm 1	
[Ne III] 15.56 μm	41 \pm 3		3.8 \pm 0.4		3.4 \pm 0.3	
[S III] 18.71 μm	87 \pm 6		3.0 \pm 0.3		3.0 \pm 0.3	
H ₂ S(1) $J = 3 - 1$ 17.03 μm	49 \pm 3		4.0 \pm 0.3		4.3 \pm 0.3	
PAH ^c 11.2 μm	1400 \pm 100	0.85 \pm 0.04	105 \pm 9	0.99 \pm 0.05	89 \pm 7	0.77 \pm 0.04
PAH 12.0 μm	85 \pm 7	0.043 \pm 0.002	2.5 \pm 0.9	0.02 \pm 0.01	4.7 \pm 0.8	0.04 \pm 0.01
PAH 12.7 μm	600 \pm 50	0.32 \pm 0.02	36 \pm 3	0.36 \pm 0.02	23 \pm 2	0.21 \pm 0.01
PAH 16.5 μm	68 \pm 5	0.08 \pm 0.01	4.0 \pm 0.5	0.08 \pm 0.01	3.6 \pm 0.4	0.08 \pm 0.01
PAH 17.4 μm	32 \pm 2	0.038 \pm 0.002	5.5 \pm 0.6	0.12 \pm 0.01	3.6 \pm 0.4	0.08 \pm 0.01

^aUnits are (10^{-17} erg cm⁻² s⁻¹ arcsec⁻²)

^bUpper limits are 3σ .

^cIntensities for the 11.2 μm feature include the secondary peak at about 11.0 μm .

Table 3. Infrared Line Intensities and PAH Equivalent Widths for GTO Data^a

	A	B	C	D	E
R.A. (J2000.0)	2 ^h 22 ^m 34.7 ^s	2 ^h 22 ^m 35.5 ^s	2 ^h 22 ^m 36.5 ^s	2 ^h 22 ^m 37.6 ^s	2 ^h 22 ^m 38.4 ^s
Decl. (J2000.0)	42° 20' 57''	42° 21' 50''	42° 22' 19''	42° 22' 46''	42° 23' 14''
Gas phase intensities ^b					
[SIV] 10.51 μm	<25 ^c	<25	<25	<25	<25
[NeII] 12.81 μm	170 \pm 14	170 \pm 14	230 \pm 18	510 \pm 40	90 \pm 7
[NeIII] 15.56 μm	21 \pm 4	23 \pm 4	32 \pm 4	66 \pm 5	<12
[SIII] 18.71 μm	40 \pm 4	43 \pm 4	64 \pm 5.3	180 \pm 30	30 \pm 4
[SIII] 33.48 μm	93 \pm 6	150 \pm 10	170 \pm 12	280 \pm 19	81 \pm 6
[SiII] 34.72 μm	160 \pm 12	220 \pm 15	260 \pm 20	330 \pm 20	100 \pm 7
H ₂ S(1) $J = 3 - 1$ 17.03 μm	41 \pm 3	36 \pm 3	40 \pm 3	51 \pm 4	24 \pm 2
PAHs intensities ^b and EWs (μm)					
PAH ^d 11.2 μm	940 \pm 80	750 \pm 60	1000 \pm 80	1300 \pm 100	740 \pm 60
	1.04 \pm 0.05	0.52 \pm 0.03	0.65 \pm 0.03	0.58 \pm 0.03	0.95 \pm 0.05
PAH 12.0 μm	< 42	< 42	< 42	< 42	< 42
	< 0.05	< 0.03	< 0.03	< 0.03	< 0.05
PAH 12.7 μm	380 \pm 30	450 \pm 40	570 \pm 45	700 \pm 60	210 \pm 17
	0.29 \pm 0.01	0.31 \pm 0.02	0.39 \pm 0.02	0.36 \pm 0.02	0.245 \pm 0.01
PAH 16.5 μm	< 19	42 \pm 8	53 \pm 8	42 \pm 8	< 19
	< 0.05	0.07 \pm 0.01	0.09 \pm 0.01	0.04 \pm 0.01	< 0.05
PAH 17.4 μm	< 17	< 17	< 17	< 17	< 17
	< 0.05	< 0.03	< 0.03	< 0.02	< 0.06

^aSpitzer program ID 97

^bUnits are (10^{-17} erg cm⁻² s⁻¹ arcsec⁻²)

^cUpper limits are 3σ .

^dIntensities for the 11.2 μm feature include the secondary peak at about 11.0 μm .

